A coupled non–saturated model for cohesionless sediment transport

Pablo Ortiz,[1] Jorge Molina,[1, a)] and Rafael Bravo[1]
University of Granada, Esc. Ing. Caminos, Campus Fuentenueva, 18071 Granada, Spain

A continuous formulation and a suitable finite element numerical method are introduced for simulating interactions between fluid flow and evolving bedforms. Sediment transport is modeled by solving the non–equilibrium saltation dynamics of non-cohesive grains. The approach integrates the Navier–Stokes equations for incompressible fluid flow, a conservation equation to track evolution of the fluid–solid interface, and mass and momentum equations governing sediment dynamics. The latter conservation laws are depth–integrated over the saltation layer, resulting in a reduced–dimensional framework that improves computational efficiency. A built–in explicit procedure enables a straightforward two–way coupling between sediment and fluid dynamics. To stabilize flow computations and ensure the positivity of key variables, such as saltation layer density and sediment thickness, the numerical algorithm is a non–oscillatory finite element method (NFEM); its positive definite characteristic is essential for flows in combined erodible/non–erodible scenarios. Numerical experiments assess the model response for transient conditions, including wind tunnel environments and sand dune–atmospheric boundary layer interactions. Among other features, test's setups are designed to explore advantages of the proposed model under severe transient conditions in comparison with results of standard saturated flow based models.

I. Introduction

When fluid flow acts on the surface of a bedform constituted by cohesionless sediment particles, the fluid threshold state [1] occurs if the bed shear stress equals the resistant limit to initiate grain motion. The threshold state is affected by the collision of grains and its stress values are regularly lower in the case of concurrent impacts. Accordingly, onset of grain motion already manifests the relevance to identify fluid–particles and particles–particles momentum exchanges. Once transport begins, it can occur in several modes: by rolling, sliding, or detaching from one contact point and sliding over another, which can be dominant for flaky particles [2]. Subsequent to the initiation of motion, bedload transport is established and saltation of particles usually prevails. Bedload transport by saltation involves phenomena such as aerodynamic entrainment and splash, comprising bed–impacting grain interaction [3], again with significant momentum transfers. While saltation progresses, a pseudo–equilibrium state currently called *saturation state* can be reached, depending on local dynamics and geometry. During *non–saturated* stages, the spatial lags in the momentum exchange due to the increase of local fluid stress cause excess of erosion and the subsequent deposition of the sediment overload [4]. As a result of this transitory stage, procedures based on pseudo–equilibrium assumptions have limitations to predict non–saturated bed dynamics. Discrepancies become noteworthy under sudden flow change conditions, typically at the brink of a dune [3].

Continuous formulation of saltation has a long history, with Bagnold's influential contribution [4] being a notable milestone for saturated transport. Bagnold's law has been recurrently adjusted over the years, as discussed in Lettau and Lettau [5], Ortiz and Smolarkiewicz [6], Durán, Andreotti, and Claudin [7], among others. Moreover, generalizations

[a)] jorgemolina@ugr.es; Corresponding author

have been proposed, including potential formulae introduced in Molina, Ortiz, and Bravo [8], that encompass both established solutions and novel approaches. This reference can be a good starting point for a thorough review, including citations therein. In Sauermann, Kroy, and Herrmann [3] authors extend saturated sand flux continuum laws to incorporate transients with a reduced set of phenomenological parameters. Despite this work has a widespread citation, its continuous formulation for non–saturated sediment flows has not been consistently adopted or further extended in the literature. A primary cause could be the challenging integration of the partial differential equations system governing the sediment transport for realistic fluid flows.

We introduce a set of differential equations to model the coupled motion of fluid and sediment under non–equilibrium saltation dynamics. The method is intended for cohesionless sediments such as sand, hence within a grain size range where cohesive forces can be neglected. The system is established by the equations of motion for a fluid flow partially enclosed by evolving landforms, and by conservation laws for the sediment flow, integrated over the saltation layer. Although drag force and grain–borne stress are computed along the lines of those produced in Sauermann, Kroy, and Herrmann [3], sediment mass and momentum laws are rewritten without restrictions for erosion rates and sediment velocities, seeking for an adequate modeling of sudden changes for coupled fluid and sediment flows over complex bedforms. The model incorporates a conservation law to track the evolution of the solid/fluid interface which also adds forcings to the fluid flow momentum through dynamic domain alterations [8,9]. Besides, the approach features a simple explicit procedure to achieve a two–way coupling between fluid flow and particles. This is accomplished by modifying the bed shear stress to incorporate the component due to the drag force exerted on the particles.

An essential constituent of this research is the numerical solution of the resulting fluid/sediment equations of motion. The solution is achieved via a finite element method (FEM) for fluid flows over erodible beds, as well as over beds composed of cohesionless and non–removable materials [9]. A key novelty is the incorporation and coupling of the depth–integrated solution for the sediment conservation laws within the saltation layer. The FEM for the complete system is a conservative and sign–preserving algorithm denominated NFEM (non–oscillatory finite element method, e.g. Ortiz [10], Ortiz, Anguita, and Riveiro [11]). These vital requisites of the procedure ensure an adequate capture of multiple evolving fronts and layers of the fluid/sediment flow by shrinking spurious residuals on interfaces during computation [12].

Section II comprises two subsections. The first subsection focuses on the formulation of the fluid flow equations and non–saturated sediment transport laws; the second one summarizes the numerical discretization procedure, with emphasis on the novel features. Section III demonstrates the versatility of the approach through various case studies and includes a discussion of the results. The paper concludes with final remarks. Appendix A reports computation of forces and sources for the saltation layer.

II. Model formulation for fluid flow and non-saturated sediment transport

A. Continuous Equations of motion

The governing equations for the flow of an incompressible fluid with density ρ_f and dynamic viscosity μ_f in a conservative form are

$$\nabla \cdot \mathbf{u} = 0 \,, \tag{1}$$

$$\frac{\partial \mathbf{u}}{\partial t} + \nabla \cdot (\mathbf{u}\mathbf{u}) = -\frac{1}{\rho_f}\nabla p + \frac{1}{\rho_f}\nabla \cdot \tau \,, \tag{2}$$

in the space domain $\Omega \in \mathbf{R}^d$ bounded by Γ, and time interval $t \in [t_0, T]$. The fluid velocity field is denoted as $\mathbf{u}(\mathbf{x}, t)$, ($\mathbf{x}$=$(x_l)$, l=$1, d$), d is the number of space dimensions, $p = p' - \rho_f g z$ is the dynamic pressure where p' is the total pressure, g is the gravity acceleration, z is the vertical coordinate, and $\tau_{ij} = \mu_f \left(\frac{\partial u_i}{\partial x_j} + \frac{\partial u_j}{\partial x_i} \right)$ is the shear stress tensor. Initial conditions for $(\mathbf{u}, p)$ are given by: $\mathbf{u}(\mathbf{x}, t_0) = \overline{\mathbf{u}}_0(\mathbf{x})$, $p(\mathbf{x}, t_0) = \overline{p}_0(\mathbf{x})$. Boundary conditions are specified as

$$\mathbf{u} = \overline{\mathbf{u}}_f, \ \frac{\partial p}{\partial \mathbf{n}_b} = 0 \ \text{ on } \ \Gamma_{\mathrm{f}}^- \qquad \text{(a)} \ ,$$

$$\mathbf{u} \cdot \mathbf{n}_b = 0, \ \mathbf{t}_b \cdot \tau \cdot \mathbf{n}_b = 0, \ \mathbf{b}_b \cdot \tau \cdot \mathbf{n}_b = 0, \ \frac{\partial p}{\partial \mathbf{n}_b} = 0 \ \text{ on } \ \Gamma_{\mathrm{s}}^- \qquad \text{(b)} \ ,$$

$$\frac{\partial \mathbf{u}}{\partial \mathbf{n}_b} = 0, \ p = \overline{p} \ \text{ on } \ \Gamma^+ \qquad \text{(c)} \ .$$

Boundary portions Γ^- and Γ^+ ($\Gamma = \Gamma^- + \Gamma^+$) refer to sections that include inlet and wall conditions ($\mathbf{u} \cdot \mathbf{n}_b \leq 0$), and sections with outlet conditions, respectively. Boundary $\Gamma^- = \Gamma_{\mathrm{f}}^- + \Gamma_{\mathrm{s}}^-$, where subscript f indicates fixed velocity condition and subscript s indicates slip condition. Overline denotes prescribed values, and vectors $\mathbf{n}_b$, $\mathbf{t}_b$, $\mathbf{b}_b$ are the normal, tangent, and bitangent to the boundary, respectively.

To establish the evolving flow domain it is necessary to determine the fluid-solid interface location. This location is computed by the companion conservation equation for the effective sediment layer thickness $h(\tilde{\mathbf{x}}, t)$, ($\tilde{\mathbf{x}} = (\tilde{x}_l)$, $l = 1, d-1$),

$$\rho^{av} \frac{\partial h}{\partial t} + \nabla_H \cdot \mathbf{q}_s = \nabla_H \cdot (\rho^{av} \mathcal{K} \nabla_H h^*) \ , \tag{3}$$

where ρ^{av} is an average bulk density of the sediment substrate, $\mathbf{q}_s$ is the sediment mass flux and operator $\nabla_H = \left(\frac{\partial}{\partial x_1}, \ldots, \frac{\partial}{\partial x_{d-1}} \right)$. Equation (3) applies within $\left(\Gamma_h \subset \Gamma_{\mathrm{f}}^- \right) \in \mathbf{R}^{d-1}$, $t \in [t_0, T]$, with initial condition $h(\tilde{\mathbf{x}}, t_0) = \overline{h}_0(\tilde{\mathbf{x}})$, and boundary condition $h = \overline{h}$ on $\partial\Gamma_h$, where the latter is the curve enclosing Γ_h. In Eq. (3) the bed vertical position $h^*(\tilde{\mathbf{x}}, t) = h_s(\tilde{\mathbf{x}}) + h(\tilde{\mathbf{x}}, t)$, where h_s is the upper location of a non–erodible layer. The avalanche flux $\rho^{av} \mathcal{K} \nabla_H h^*$ acts as a natural slope limiter. This term is computed as an anisotropic diffusion with diffusivity $\mathcal{K} \equiv \beta \left[\max \left(0, \mathrm{sgn} \left(\| \nabla_H h^* \| - s_C \right) \right) \right]$, where $s_C = \tan \alpha$ is the critical slope and α is the angle of friction; consequently $\mathcal{K}$ depends critically on the bed slope. The coefficient β is stated by the temporal and spatial resolution of the numerical model [13].

The integration of mass and momentum equations for the sediment flow over the thickness of the saltation layer results in the sediment conservation laws proposed. Final system is written in a conservative form as

$$\frac{\partial \rho_s}{\partial t} + \nabla_H \cdot \mathbf{q}_s = R_s \tag{4}$$

$$\frac{\partial \mathbf{q}_s}{\partial t} + \nabla_H \cdot (\mathbf{q}_s \mathbf{v}) = \mathbf{F}_s \ , \tag{5}$$

in Γ_h, $t \in [t_0, T]$, where $\rho_s(\tilde{\mathbf{x}}, t)$ denotes the depth–integrated bulk density of the saltation layer, and $\mathbf{v}(\tilde{\mathbf{x}}, t)$ is the depth–integrated velocity of the sediment particles in the saltation layer. Sediment mass flux is then established as $\mathbf{q}_s = \rho_s \mathbf{v}$. Mass source R_s is the erosion/deposition rate of grains mobilized per time and area, assessed as the balance between flux of particles uplifting the bed and flux of particles impacting it. In Eq.(5) the force applied to the sediment layer is designated as $\mathbf{F}_s$. This force is the resultant of the drag exerted on the sediment particles by the fluid flow, the force ascribable to the grain borne shear stress field, and the gravity component as a pressure type force, active if the bed is non–horizontal. By incorporating Eq. (4) in Eq. (5), an alternative to momentum conservation is

$$\frac{\partial \mathbf{v}}{\partial t} + \mathbf{v} \cdot \nabla_H \mathbf{v} = \frac{1}{\rho_s} \left[\mathbf{F}_s - R_s \mathbf{v} \right] \ . \tag{6}$$

The term $R_s\mathbf{v}$ can be thought as the instantaneous momentum of the mobilized grains for the non–saturated state. It is noteworthy that Eq. (6) reduces to Eq. (2) in Sauermann, Kroy, and Herrmann [3] if $R_s\mathbf{v}$ is negligible; hence for small erosion rates and/or reduced sediment velocities. The Appendix A encompasses the computation of R_s and $\mathbf{F}_s$.

Owing to sediment motion, the fluid domain is continuously adapted to follow the evolving fluid-sediment interface (Eq. (3)). This transformation is accomplished through a surface-tracking methodology [8,9]. While these domain modifications introduce a forcing effect on the flow, the current set of equations does not account for fluid momentum reduction by its partial transfer to the grains. To circumvent this restriction, a *two–way* coupling procedure is introduced by computing the fluid–bed shear stress as $\tau_b = \tau \cdot \mathbf{n}_b - \mathbf{F}_s^*$, where $\mathbf{F}_s^*$ is the integrated drag force exerted on saltation layer grains (first term of the right hand side in Eq. (A2)). The boundary values of the shear stress components τ_b are specified via a standard weak form term in the finite element solution of Eq. (2).

B. Numerical Solution

Several numerical methods have been applied to sediment transport and bedform dynamics at very different spatial and time scales. Examples include, among others, the Discrete Element Method (DEM), which has been applied to study incipient motion at microscale [1]; PFEM-2, which enabled the simulation of large-scale dune and trench formation [14]; finite difference methods with coordinate transformation for fluid flow and sediment transport past evolutionary sand dunes [6], fully coupling flow aloft with the developing landform; or coupled CFD–DEM to reproduce turbulence-driven sediment transport and dune morphology [15,16]. Nevertheless, none of the prevailing methods integrates the system of transient differential equations in the form of depth–integrated conservation laws to model non–saturated conditions of saltation transport. In this section we shall focus on the numerical solution by the NFEM of the depth–integrated system of equations over the saltation layer. For details on the formulation of the numerical solution for the governing equations of the fluid dynamics, we suggest the reader to check the references cited in the Introduction.

The non–oscillatory finite element method (NFEM) performs the numerical integration of Eqs. (1)–(5) employing flux correction techniques to attain a conservative and sign–preserving solution. The fundamentals of the algorithm rest on the correction of a conservative and sign–preserving predictor low order procedure (LO) with anti–diffusive contributions. Corrections are calculated by limiting the difference between contributions of a high order method (HO) and those of the predictor method. The formulation of high and low order solutions for Eqs. (1)–(2) and Eq. (3) were reported in previous works [8,9,11].

High order solutions for Eqs. (4)–(5) are obtained by the Characteristic Galerkin method and is stated in terms of the finite element spaces $\mathcal{S}^h$, and $\mathcal{R}^h$, $\mathcal{M}_i^h$ and $\mathcal{Q}_i^h$ $(i = 1, d-1)$, defined as

$$\mathcal{S}^h \subset \mathcal{S} = \{s \in H^1(\Gamma_h) \mid s = 0 \text{ on } \partial\Gamma_h\} \,,$$

$$\mathcal{R}^h \subset \mathcal{R} = \{\rho_s \in H^1(\Gamma_h) \mid \rho_s = \overline{\rho}_s \text{ on } \partial\Gamma_h\} \,,$$

$$\mathcal{M}_i^h \subset \mathcal{M}_i = \{m_i \in H^1(\Gamma_h) \mid m_i = 0 \text{ on } \partial\Gamma_h\} \,,$$

$$\mathcal{Q}_i^h \subset \mathcal{Q}_i = \{q_{s,i} \in H^1(\Gamma_h) \mid q_{s,i} = \overline{\mathbf{q}}_{s,i} \text{ on } \partial\Gamma_h\} \,.$$

Solution is formulated as: Find $(\rho_s^h)^{n+1} \in \mathcal{R}^h$ and $(q_{s,i}^h)^{n+1} \in \mathcal{Q}_i^h$ for all $t \in [t_0, T]$, such

that

$$\left(s^h, \frac{\Delta\rho_s^h}{\Delta t}\right)_{\Gamma_h} = \left((\mathbf{v}^h)^{n+1/2}\cdot\nabla_H s^h, (\rho_s^h)^n\right)_{\Gamma_h} - \left[s^h, \overline{\rho}_s\overline{\mathbf{v}}\right]^n_{\partial\Gamma_h^+} + \left(s^h, R_s\right)^n_{\Gamma_h}$$
$$-\frac{\Delta t}{2}\left\{\left\langle\nabla_H\cdot\left(s^h\left(\mathbf{v}^h\mathbf{v}^h\right)^{n+1/2}\right), \nabla_H(\rho_s^h)^n\right\rangle_{\Gamma_{hI}} - \left\langle s^h\left((\mathbf{v}^h)^{n+1/2}\cdot\nabla_H(\mathbf{v}^h)^n\right), \nabla_H(\rho_s^h)^n\right\rangle_{\Gamma_{hI}}\right.$$
$$\left. + \left(\nabla_H\cdot s^h(\mathbf{v}^h)^{n+1/2}, \left(\rho_s^h\nabla_H\cdot\mathbf{v}^h\right)^n\right)_{\Gamma_{hI}} + \left(s^h, (\mathbf{v}^h)^{n+1/2}\cdot\nabla_H(R_s)^n\right)_{\Gamma_{hI}}\right\}\ , \quad (7)$$

$$\left(m_i^h, \frac{\Delta q_{s,i}^h}{\Delta t}\right)_{\Gamma_h} = \left((\mathbf{v}^h)^{n+1/2}\cdot\nabla_H m_i^h, (q_{s,i}^h)^n\right)_{\Gamma_h} - \left[m_i^h, \overline{q}_{s,i}\overline{\mathbf{v}}\right]^n_{\partial\Gamma_h^+} + \left(m_i^h, F_{s,i}\right)^n_{\Gamma_h}$$
$$-\frac{\Delta t}{2}\left\{\left\langle\nabla_H\cdot\left(m_i^h\left(\mathbf{v}^h\mathbf{v}^h\right)^{n+1/2}\right), \nabla_H(q_{s,i}^h)^n\right\rangle_{\Gamma_{hI}} - \left\langle m_i^h\left((\mathbf{v}^h)^{n+1/2}\cdot\nabla_H(\mathbf{v}^h)^n\right), \nabla_H(q_{s,i}^h)^n\right\rangle_{\Gamma_{hI}}\right.$$
$$\left. + \left(\nabla_H\cdot m_i^h(\mathbf{v}^h)^{n+1/2}, \left(q_{s,i}^h\nabla_H\cdot\mathbf{v}^h\right)^n\right)_{\Gamma_{hI}} + \left(m_i^h, (\mathbf{v}^h)^{n+1/2}\cdot\nabla_H(F_{s,i})^n\right)_{\Gamma_{hI}}\right\}\ , \quad (8)$$

where $(\rho_s^h)^{n+1} = (\rho_s^h)^n + \Delta\rho_s^h$, $(q_{s,i}^h)^{n+1} = (q_{s,i}^h)^n + \Delta q_{s,i}^h$, $\mathbf{v}^h = \mathbf{q}_s^h/\rho_s^h$, $\overline{\mathbf{v}} = \overline{\mathbf{q}}_s/\overline{\rho}_s$, $\partial\Gamma_h^+$ is the portion of the bedform boundary with a prescribed sediment mass flux $\overline{\mathbf{q}}_s$ with density $\overline{\rho}_s$, Γ_{hI} is the bedform domain without elements with sides belonging to the boundary, and

$$(v,w)_{\Gamma_h} = \int_{\Gamma_h} v\,w\ \mathrm{d}\Gamma_h\ ,\quad \langle\mathbf{v},\mathbf{w}\rangle_{\Gamma_h} = \int_{\Gamma_h}(\mathbf{v}\cdot\mathbf{w})\ \mathrm{d}\Gamma_h \ \text{ and } \ [v,\mathbf{c}]_{\partial\Gamma_h} = \int_{\partial\Gamma_h} v\,\mathbf{c}\cdot\mathbf{n}_b\ \mathrm{d}\partial\Gamma_h\ .$$

Low order solution is computed with an upwind scheme and is formulated as: Find $(\rho_s^h)_{LO}^{n+1} \in \mathcal{R}^h$ and $(q_{s,i}^h)_{LO}^{n+1} \in \mathcal{Q}_i^h$ for all $t \in [t_0, T]$, such that

$$\left(s_L^h, \frac{\Delta({\rho_s}^h)_{LO}}{\Delta t}\right)_{\Gamma_h} = \left(s^h, \mathcal{LO}\left((\rho_s^h)^n, (\mathbf{v}^h)^n\right)\right)_{\Gamma_h} + \left(s_L^h, R_s\right)^n_{\Gamma_h}\ , \quad (9)$$

$$\left(m_{L,i}^h, \frac{\Delta(q_{s,i}^h)_{LO}}{\Delta t}\right)_{\Gamma_h} = \left(m_i^h, \mathcal{LO}\left((q_{s,i}^h)^n, (\mathbf{v}^h)^n\right)\right)_{\Gamma_h} + \left(m_{L,i}^h, F_{s,i}\right)^n_{\Gamma_h}\ , \quad (10)$$

where functions s_L^h, $m_{L,i}^h$ correspond to the lumped mass matrices. Predictor solutions are defined as $(\rho_s^h)_{LO}^{n+1} = (\rho_s^h)^n + \Delta(\rho_s)_{LO}^h$, $(q_{s,i}^h)_{LO}^{n+1} = (q_{s,i}^h)^n + \Delta(q_{s,i}^h)_{LO}$, and $\mathcal{LO}()$ indicates the low order operator comprising computation of upwind fluxes (for the full rationale of the low order operator, see Ortiz[17], Section 3.1, and Molina, Ortiz, and Bravo[9], Section 2.2.1).

The corrected solution $(\tilde{\mathbf{q}}_s, \tilde{\rho}_s)_{(k)}$ at node k of the finite element mesh at time $(n+1)\Delta t$ is

$$(\tilde{\mathbf{q}}_s, \tilde{\rho}_s)_{(k)}^{n+1} = (\mathbf{q}_s, \rho_s)_{LO(k)}^{n+1} + \sum_{j=1}^{e}\tilde{\mathbf{A}}_{(j)} = (\mathbf{q}_s, \rho_s)_{LO(k)}^{n+1} + \sum_{j=1}^{e}\mathbf{c}_{(j)}\mathbf{A}_{(j)}$$

$$= (\mathbf{q}_s, \rho_s)_{LO(k)}^{n+1} + \sum_{j=1}^{e}\mathbf{c}_{(j)}(\mathbf{A}_{HO} - \mathbf{A}_{LO})_{(j)}\ , \quad (11)$$

where $\tilde{\mathbf{A}}_{(j)}$ are corrected anti–diffusive contributions of element j, e is the total number of elements j surrounding node k, and $\mathbf{c}_{(j)}$'s are elementwise correcting functions. The correcting functions depend on nodal high order solution, nodal low order solution, and

the element contribution to the node of the m variables of the problem, written as $\mathbf{A}_{(j)}$. Range of $\mathbf{c}_{(j)}$'s is: $0 \leq c_{(j)m} \leq 1$, $c_{(j)m} \in \mathbf{c}_{(j)}$, and $(m = 1, 3)$ for Eqs. (4)–(5). For $c_{(j)m}$=1 element contribution corresponds to the difference between high order contribution $\mathbf{A}_{HO(j)}$ and low order contribution $\mathbf{A}_{LO(j)}$, and corrected solution equals the high order solution; for $c_{(j)m}$=0 the solution equals the low order solution. A comprehensive formulation of the flux correction algorithm is reported in Ortiz [17].

The Finite Element model is coded in C++, and its 3D version has been parallelized with MPI (Message Passing Interface) and OpenMP (Open Multi-Processing). The algorithm has the following steps: (i) root process reads the grid structure used for the fluid and sediment solutions; (ii) meshes are partitioned in the X-Y plane into N subdomains, where N corresponds to the number of computational cores available; (iii) each core receives data of all nodes and elements within its domain, in addition to data of 'shared' elements (those with at least one node belonging to the subdomain), and external nodes linked to its domain. With this information, each core is able to get local nodal vectors resulting from the computation of the right hand side of the sets of equations involved in the fluid and sediment solutions. These sets of equations are solved by a semi–explicit procedure, employing a Preconditioned Conjugate Gradient (PCG), which also allows for MPI parallelization as coefficient matrix does not have to be assembled.

III. Results and Discussion

A. Dynamics of the saltation layer under constant shear velocity

We reproduce the experiments in Sauermann, Kroy, and Herrmann [3], where a constant shear stress acts on a rectangular flat surface of 10 m long and 0.27 m wide. The bed is composed by grains with material density $\rho_m = 2650$ kg/m^3 and mean diameter $D = 2.5 \times 10^{-4}$ m. Bed roughness is $z_0 = 2.5 \times 10^{-5}$ m, threshold shear velocity $u_t = \sqrt{\tau_t/\rho_f} = 0.28$ m/s where τ_t is the threshold shear stress, and drag coefficient $C_d = 3.0$. According to Sauermann, Kroy, and Herrmann [3], saltation layer has a total thickness z_m=0.04 m and z_1=0.005 m (see Appendix A). The domain is discretized in 1.4×10^4 triangular finite elements with an average size $\delta = \sqrt{\sum_{i=1}^{n} A_i/N} = 0.014$ m, where A_i is the area of element i, and N is the total number of elements. Time step for the integration of the discrete sediment mass and momentum equations (7)–(10) is $\Delta t = 2.0 \times 10^{-4}$ s.

Three tests are considered. First test studies the sediment flux evolution at a specific location. Restitution and relaxation coefficients are α=0.35 and γ=0.4, respectively, and advective terms in equations (4) and (5) are not included. Further, we prescribe $\rho_s(t_0)$=10^{-5} kg/m^3 to promote the formation of the saltation layer. Aerodynamic entrainment is deactivated at the first stage of the experiment.

Figure 1 shows the history $q_s(t)$ for u_*=$|\mathbf{u}_*|$ ranging from 0.4 to 0.7 m/s, where $\mathbf{u}_*$ denotes the friction velocity. Sediment flux increases exponentially due to multiplication effect caused by the saltation up to a peak where grains velocity is above of that corresponding to the saturated state. Afterwards a significant amount of energy is lost, quantified by the restitution coefficient and the erosion intensity, saltation activity decreases and eventually velocity and density attain saturation levels. As the shear velocity increases, the peak becomes more pronounced, saturated flux rises, and saturation time decreases. Saturation time is highly dependent on the initial sediment density. Whether we increase the value of $\rho_s(t_0)$ or activate the aerodynamic entrainment rate term and set $\rho_s(t_0)$=0, the saturation time decreases importantly. This decrease is consistent with that observed due to shear stress augmentation. Peaks in sediment flux are moderately attenuated and saturation times are shorter in compare with those of Sauermann, Kroy, and Herrmann [3], as a consequence of the conservative momentum equation usage, equivalent to include the term $-R_s\mathbf{v}/\rho_s$ on the right hand side of the non–conservative momentum equation proposed in Sauermann, Kroy, and Herrmann [3] (see Eq. (6)). Added source reduces maximum velocity, leading up

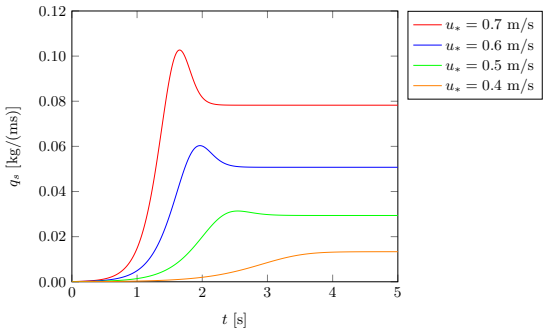

Figure 1: Evolution of sediment flux at a specific location under several constant shear velocities.

to peak flux and characteristic time reductions. In the latter case, note that this time is proportional to velocity and inverse to the wall shear stress $\tau_*{=}\rho_f \left|\mathbf{u}_*\right|^2$ (see e.g. Eq.(31) in Sauermann, Kroy, and Herrmann [3]).

Second test examines the sediment flux spatial behavior once a pseudo–stationary state is achieved. Here grains of the saltation layer have a constant velocity corresponding to saturated conditions. This value is calculated by setting $\mathbf{F}_s{=}0$ in Eq. (A2) and by considering $\rho_s{=}\frac{2\alpha}{g}(\tau_* - \tau_t)$. The pseudo–stationary grain velocity $\mathbf{v}_{st}$ is given by Sauermann, Kroy, and Herrmann [3],

$$\mathbf{v}_{st} = \mathbf{v}_{st}(\mathbf{u}_*) = \frac{2\mathbf{u}_*}{\kappa}\sqrt{\frac{z_1}{z_m} + \left(1 - \frac{z_1}{z_m}\right)\frac{u_t^2}{\left|\mathbf{u}_*\right|^2}} - \frac{2u_t}{\kappa} + \mathbf{u}_{st}\,, \tag{12}$$

$$\mathbf{u}_{st} = \frac{\mathbf{u}_*}{\left|\mathbf{u}_*\right|}\left(\frac{u_t}{\kappa}\ln\frac{z_1}{z_0} - \sqrt{\frac{2gD\rho_m}{3\alpha C_d \rho_f}}\right)\,. \tag{13}$$

Density and velocity of grains are uncoupled and only Eq. (4) is solved until steady–state. Relaxation coefficient $\gamma{=}0.2$. Results are depicted in Fig. 2 for shear velocities from 0.4 to 0.7 m/s. In this scenario sediment flux peak vanishes, and flux tends to saturation without over–saturated densities. Outputs match to a high degree with those reported in Sauermann, Kroy, and Herrmann [3].

Third test incorporates advective terms not taken into account by Equations (12)–(13). The neglect of these accelerations produces significant deviations, as illustrated in Fig. 3. These outputs are derived by solving equations (7)–(8), where source term R_s contains erosion due to the aerodynamic entrainment.

Results shown in Fig. 3a are established by defining a relaxation coefficient of 0.4. Under this condition, sediment flux exhibits an oscillatory behavior for $u_*{=}0.5$, 0.6 and 0.7 m/s because the saturation density is not consistently maintained over time. In these cases, when grains' velocity is low and the density is below its saturation value, the effective velocity (Eq. (A3)) rises considerably, resulting in an increase of grains' velocity. Simultaneously, density also rises as source is inversely proportional to grain velocity (see Eq. (A1)). Hence a major growth of the sediment flux is caused, reaching an oversaturated density value and elevated grains' velocity. Further, effective velocity and source decrease, and also sediment flux, restoring initial conditions and leading to a pseudo–periodic process. In Fig. 3b we present the results of the same experiment, now for $\gamma{=}0.8$, sufficient to dissipate oscillations in the selected range of shear velocities by altering density responses to perturbations.

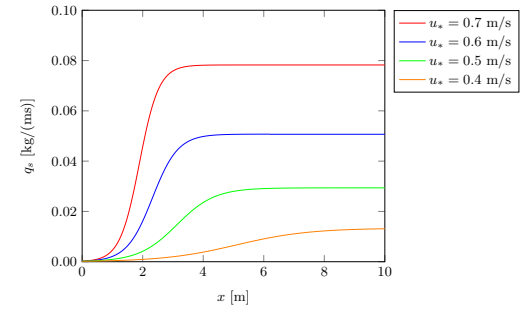

Figure 2: Spatial distribution of sediment flux on a flat surface under several constant shear velocities, using a simplified set of equations.

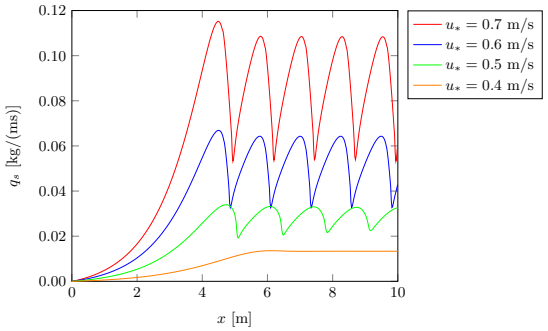

(a) Results for $\gamma = 0.4$

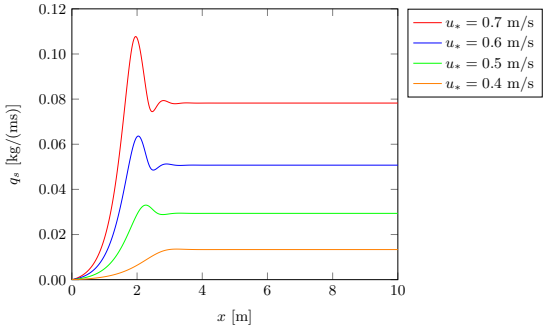

(b) Results for $\gamma = 0.8$

Figure 3: Spatial distribution of sediment flux on a flat surface under several constant shear velocities, using the complete set of equations. Results are shown for relaxation coefficients $\gamma = 0.4$ and $\gamma = 0.8$.

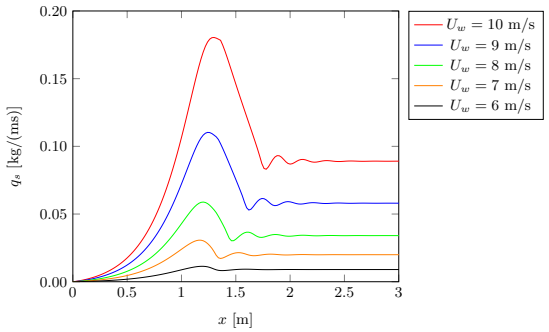

Figure 4: Spatial distribution of sediment flux assuming that flow at the inlet is clean.

B. Sediment flux evolution under sudden changes in boundary conditions

We examine the response of the saltation layer to variations in fluid flow, bedform topology, and to transitions between erodible and non–erodible strata. Test set-up is the same as in III A, although here the sediment has a mean diameter of D=2.0×10^{-4} m and shear velocity threshold u_t=0.20 m/s, to reproduce parameters chosen in the experiments of Selmani *et al.*[18]. Five wind inlet velocities specify this series of test, U_w=10, 9, 8, 7 and 6 m/s. The corresponding saturated sediment fluxes stated in Selmani *et al.*[18] are $|\mathbf{q}_{\rm sat}| = 0.089$, 0.058, 0.034, 0.020 and 0.009 kg/(ms). A correlation between shear velocity and wind velocity is calculated as u_*=0.1109 U_w-0.2994 m/s, resulting from Eqs. (12)–(13), as well as taking into account that $\mathbf{q}_{\rm sat} = \rho_{\rm sat}\mathbf{v}_{st}$, where $\rho_{\rm sat} = \frac{2\alpha}{g}(\tau_* - \tau_t)$.

Experiment starts with the case of a clean fluid inflow. Its results are shown in Fig. 4 as $q_s(x)$, coming from the solution of Eqs. (7)–(8) with $\gamma = 0.5$, sufficient to avoid oscillations discussed in III A, and to achieve saturation lengths similar to those reported by Selmani *et al.*[18]. Sediment fluxes distribution are similar to those depicted in Fig. 3b; however saturation lengths are considerably shorter because of the reductions of grain diameter and velocity threshold.

Next, we assess the behavior of the saltation layer when the incoming sediment flux rate is non–zero and differs from the saturation rate. We set the initial sediment flux rate as $|\mathbf{q}_s| = 0.0356$ kg/(ms) to encompass three feasible scenarios: when the current saturated sediment flux is higher than, approximately equal to, and lower than the incoming sediment flux. For an evolving bedform, it should be noted that spatio–temporal variations of sediment flow, of saturation values, and of stress field can be concurrent. For instance, flow passing over the crest of a dune leads to a reduction in flow velocity and shear stress on its lee side causing a decrease in the sediment flux rate.

Figure 5 features substantial decreases of saturation length attributable to non–zero incoming sediment grains velocity for all the cases, in compare with lengths depicted in Fig. 4. As wind velocity decreases, peaks are less prominent (U_w=10, 9 m/s), while for 8 m/s the peak nearly vanishes. For U_w=7, 6 m/s, saturated sediment fluxes fall below the incoming values and peaks disappear. In compare with results in Selmani *et al.*[18], shorter times to reach the maximum peak and the saturation state were found. This discrepancy arises from the laboratory set-up used in Selmani *et al.*[18]. There, sediment is introduced via a hopper positioned at the top of the wind tunnel. Contrary to the assumption of this work, in the lab the grains were not injected directly into the saltation layer, but into the upper region of the flow instead. Consequently, grains follow a ballistic trajectory and then enter the saltation layer. The downstream distance of this trajectory is estimated as $x' \approx U_w\sqrt{2h_r/g}$ where h_r=0.27 m is the tunnel roof height. The distance $x' \approx 0.24\,\mathrm{s}\ U_w$ coincides with the

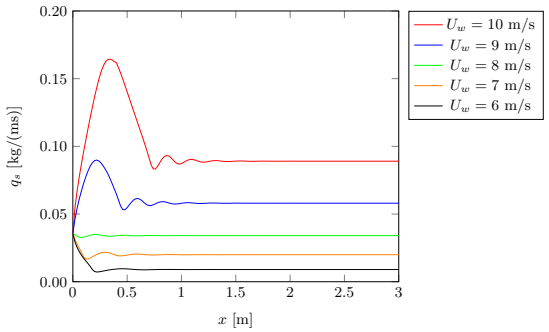

Figure 5: Spatial distribution of sediment flux assuming an initial inlet rate of 35.6 g/(ms).

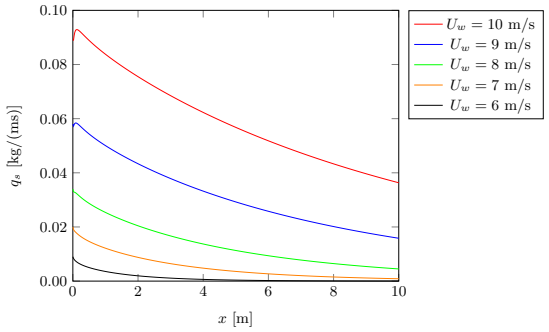

Figure 6: Spatial distribution of sediment flux over a non erodible layer for $x \geq 0$

position where the maximum sediment flux was measured in their laboratory setup.

The third test evaluates the behavior of sediment flux when a transition to a non–erodible bedform occurs, equivalent to increase the threshold shear stress such that $\tau_t \to \infty$. Figure 6 shows $q_s(x)$ if a non–erodible bed is placed for $x \geq 0$, for the complete series of wind inflow velocity. The incoming sediment fluxes ($x = 0$) are the saturated fluxes specified for the inflow wind velocities. Source term in Eq. (A1) shrinks to $R_s = -\gamma g \rho_s / (2\alpha \, |\mathbf{v}|)$, leading to a decrease in the saltation layer density. Density reduction can cause an increase in the effective velocity and in the velocity of the remaining grains in the saltation layer. As a result, for $U_w > 8$ m/s sediment flux exhibits a slight rise before the diminishing. Further these small regions, the decrease is continuous for all cases and the distances to reach zero value are considerably larger than saturation lengths shown in Fig. 4. It is remarkable that this process can not be replicated using the simplified set of equations (4), (12) and (13). The abridged model assumes an immediate grains' stationary velocity and an abrupt drop of sediment flux to zero, failing to capture the gradual reduction observed by using complete equations.

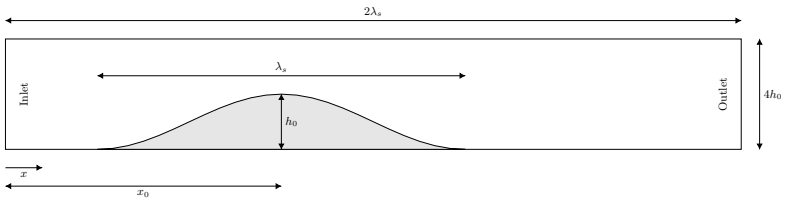

Figure 7: Layout of the dune's evolution simulation.

C. Evolution of a dune

The evolution of an isolated dune in an uniform ambient wind was examined in Molina, Ortiz, and Bravo [9] by saturated sediment flux models. To enhance results during non–saturated transients and, in particular, to shrink nonphysical material deposition at the windward foot of the dune, we conducted a simulation of the isolated dune with the complete model. Figure 7 sketches the initial shape of the bedform as a cosine sandpile with height $h(r)$ defined as

$$h(r) = \begin{cases} h_0 \cos^2(\dfrac{\pi r}{\lambda_s}) & \text{if } 2r/\lambda_s \leq 1 \\ 0 & \text{if } 2r/\lambda_s > 1 \end{cases} . \tag{14}$$

with h_0=7.5 m, λ_s=100 m, r=$|x - x_0|$, and x_0=75 m. Sandpile is composed by well sorted quartz sand sediment with bulk density ρ^{av} = 1325 kg/m^3, while sediment particles have a mean diameter D = 0.4 mm. Wind of density ρ_f=1.205 kg/m^3 and dynamic viscosity μ_f=1.808×10^{-5} kg/(ms) enters the domain on the left boundary with uniform velocity $\mathbf{u}_e$= (11 m/s, 0).

Boundary conditions are defined as follows: on the upper and lower (fluid/sediment interface) boundaries, slip ($\mathbf{u} \cdot \mathbf{n}_b = 0$) and no-slip ($\mathbf{u} = 0$) conditions are imposed, respectively, and outlet condition ($p = 0$, $\partial p/\partial \mathbf{n}_b = 0$) is prescribed at the right boundary. On the other hand, for the sediment transport solution we impose clean inflow conditions ($\rho_s = 0$, $\mathbf{v} = 0$, $h = 0$) at the left boundary, and free conditions ($\partial \rho_s/\partial \mathbf{n}_b = 0$, $\partial \mathbf{v}/\partial \mathbf{n}_b = 0$, $\partial h/\partial \mathbf{n}_b = 0$) at the right boundary. The domain is discretized using linear triangular finite elements with average element length δ=0.197 m, and the time step is $\Delta t = 1.5 \times 10^{-3}$ s, sufficient to satisfy CFL condition for both systems of equations.

Parameters for the saltation layer dynamics model are $u_t = 0.22$ m/s, $\gamma = 0.8$, and $\alpha = 0.9$. The value of α has been calibrated to match saturated sediment fluxes predicted by Lettau's law [5] within the range of friction velocities of the test. To accelerate the simulation, sediment fluxes are scaled by a time multiplier of 1440 (number of minutes per day) to solve equation (3), assuming that time scale of flow variability is much shorter than that for the dune evolution [13].

Main results are condensed in Fig. 8. The upper figure 8 shows the dune evolution assuming a saturated sediment model based on Lettau's law [5], while the lower figure 8 shows results according to the full model. In the latter, it is apparent the absence of unrealistic sediment deposition at the windward foot of the dune for the whole simulation. In the saturated flux option, the diminution in shear stress produces a sediment flux decrease, hence deposition at this region. However, in the non–saturated case, the sediment flux remains virtually zero until reaching the dune foot, consistent with the fact that there is no upwind sediment transported by the wind. Dune celerity is very similar in both cases. Estimated value is approximately 1.9–2.0 m/day. Dune length is around 66 m, while the saturated law produces a length of approximately 70 m. This deviation is probably caused by the additional sediment contribution at the dune foot produced by the saturated flow model. No traces of spurious erosion/deposition are observed in the lower non–erodible stratum, as

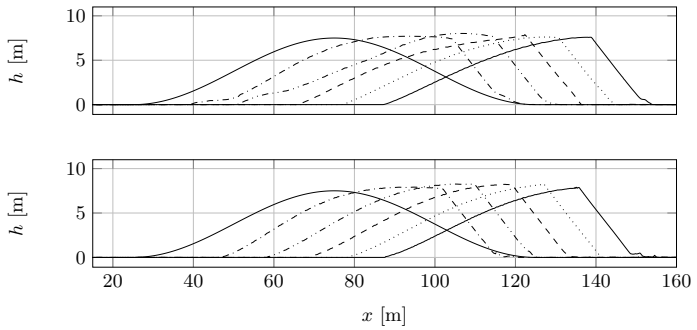

Figure 8: Evolution of an isolated dune: comparison between the simulation using saturated sediment fluxes from Lettau's law[5] (top) and non–saturated fluxes obtained by solving Eqs. (4)–(5) (bottom). The time interval between profiles is $\Delta t = 100$ h.

a consequence of the usage of a strictly positive definite conservative numerical model.

IV. Final remarks

The model presented in its complete form accurately handles the simulation of scenarios with highly varied erosion rates and particle velocities, without constraints on transients to quasi–steady states. The contribution of an affordable two way coupling between fluid and sediment dynamics is a relevant factor in ensuring these scopes. Furthermore, the conservative non–oscillatory finite element method (NFEM) plays a key role to obtain stable solutions for fluid and sediment flows, but also its strict positive definite attribute is essential for the prediction of fluid flows and cohesionless sediment transport past combined erodible and non–erodible strata.

Several archetypical scenarios for the saltation layer evolution are scrutinized. For saturation progression in clean wind conditions over flat erodible beds, results substantiate transient oversaturated stages along the initial segment of the leeward area. This effect is due to high grain velocity concurrent with a small number of moving particles in the saltation layer, remaining high even as density increases. The interaction between a fast growth of density and high sediment velocity can result in an oscillatory flux. However, transient response is sensitive to erosion intensity and restitution coefficients. Additionally, when incoming sediment flux is non–zero, oversaturated peaks diminish distinctly and tend to vanish if fluxes are close to the saturated limit.

The method's broad applicability can be illustrated with two examples. First, in problems with complex local transient dynamics ascribable to major alterations of geometry and stress field. In this case, the procedure prevents nonphysical sediment contributions that might result from assuming a permanent saturated flow. This is demonstrated in the study of the migration of a barchan dune, where all traces of spurious deposition were eliminated. Second, when applied at geomorphological and engineering scales, the method remains computationally feasible by assuming a severe wind scenario[6]. This premise effectively narrows the time–scale gap between the scales characteristic of planetary boundary flows and those of sand bedforms evolution—much like increasing fluid density, as seen in several laboratory studies (e.g. Groh *et al.*[19]). Addressing the interactions of evolving complex bedforms at the modeling detail of this work is a challenge that exceeds the scope of the current paper and will be explored in future work.

Acknowledgments

The research was supported by the Grant #PID2020-115778GB-I00 funded by MCIN/AEI/10.13039/501100011033

Data Availability Statement

The data that support the findings of this study are available from the corresponding author upon reasonable request

The source code of the numerical model presented in this article is publicly available in the GitHub repository: `https://github.com/JAMolina90/Dune_NonSaturated.git`

Authors Declarations

The authors have no conflicts to disclose

Appendix A: Computation of forces and sources in the saltation layer

Mass source in Eq. (4) is stated as

$$R_s = \gamma \frac{\tau_{g0}}{|\mathbf{v}|} \left[\frac{\tau_* - \tau_t}{\tau_t} - \frac{\tau_{g0}}{\tau_t} \right] + \Phi_a \max\left(\frac{\tau_* - \tau_{g0}}{\tau_{tf}} - 1 \, , \, 0 \right) . \tag{A1}$$

The threshold shear stress τ_t incorporates the influence of the angle between local flow current direction and slope [13]. Grain borne shear stress at the ground is calculated as $\tau_{g0}{=}\frac{\rho_s g}{2\alpha}$ where α is the effective restitution coefficient [3]. In the second term, Φ_a is the intensity of erosion due to aerodynamic entrainment, and τ_{tf} is the threshold for the fluid borne shear stress. We customarily use $\Phi_a = 5.7{\times}10^{-4}$ kg/m^{2}s and $\tau_{tf}{=}1.25\,\tau_t$ [4,20]. Finally, parameter γ measures the intensity of erosion due to grain interactions on the bed. It determines how fast the system reaches the equilibrium or reacts to perturbations [3]. Since this parameter is hardly quantifiable, it is typically adjusted to reproduce saturation times and lengths consistent with experimental observations.

The force exerted on the sediment layer denoted as $\mathbf{F}_s$ in Eq. (5) is the sum of drag, resultant of the grain borne shear stress field, and gravity. In highly confined systems or flows with strong relative accelerations (e.g. fluidized beds injected with gas), virtual mass and Saffman forces can be significant [21]. Such conditions are not encountered in the saltation layer. Then, along a typical saltation length l_s, the average vertical linear momentum of the grains ejected from the ground, the drag vertical component, and the virtual mass and Saffman forces are assumed small in compare with the horizontal components included in the right hand side of Eq. (A2). Besides, fluid pressure $p(z{=}h^*{+}\overline{z}_m){\approx}p(z{=}h^*)$, where $\overline{z}_m$ is the average thickness of the saltation layer over l_s. Hence sediment pressure p_s in a continuum saltation layer behaves in accordance with $\frac{\partial p_s}{\partial z} \approx -\rho g$, giving $p_s(z) = \rho g(h^*{+}\overline{z}_m{-}z)$. As a result, horizontal pressure force $\mathbf{F}_p = -\rho_s g \nabla_H (h^* + \overline{z}_m)$ acts when saltation layer is established, i.e. $\tau_* > \tau_t$. Resultant force is written as

$$\mathbf{F}_s = \frac{3}{4} C_d \rho_s \frac{\rho_f}{\rho_m} \frac{1}{D} \left(\mathbf{u}_{\text{eff}} - \mathbf{v}\right) |\mathbf{u}_{\text{eff}} - \mathbf{v}| - \tau_{g0} \frac{\mathbf{u}_*}{|\mathbf{u}_*|} - \rho_s g \nabla_H (h^* + \overline{z}_m) \max\left(\text{sgn}(\tau_* - \tau_t), 0\right) . \tag{A2}$$

Here C_d denotes the drag coefficient, the density of the quartz $\rho_m{=}2650$ kg/m^3, D is the average grain diameter, and $\mathbf{u}_{\text{eff}}$ is the effective fluid velocity. Along the lines of Sauermann,

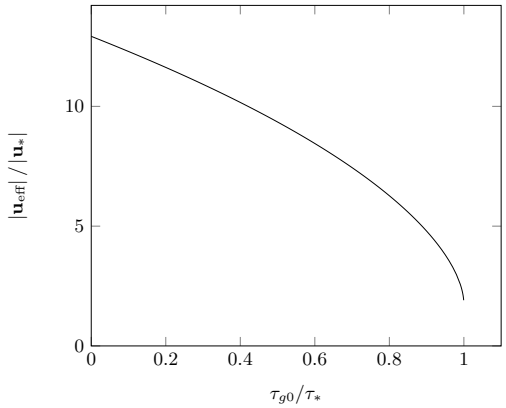

Figure 9: Non dimensional effective velocity as a function of the rate between the grain borne and the overall shear stresses. We have used $\alpha = 0.35$, $z_1 = 0.005$, $z_m = 0.04$ and $z_0 = 2.5 \times 10^{-5}$.

Kroy, and Herrmann [3] the effective fluid velocity is computed as

$$\mathbf{u}_{\text{eff}} = \frac{\mathbf{u}_*}{\kappa}\sqrt{1-\frac{\tau_{g0}}{\tau_*}}\left(2A_1 - 2 + \ln\frac{z_1}{z_0}\right),\ A_1 = \sqrt{1+\frac{z_1}{z_m}\frac{\tau_{g0}}{\tau_* - \tau_{g0}}}\,, \tag{A3}$$

where κ=0.41 is the Von Karman constant, z_1 is a reference height estimated as a free phenomenological parameter, and z_0 is the bed roughness assumed as a fraction of the grain diameter [1,22]. The effective velocity is not defined in the range $\rho_s > \frac{2\alpha}{g}\tau_*$ (or $\tau_{g0} > \tau_*$) (Fig. 9); observe that when $\tau_{g0} \to \tau_*$,

$$\lim_{\tau_{g0}\to\tau_*} \mathbf{u}_{\text{eff}} = 2\frac{\mathbf{u}_*}{\kappa}\sqrt{\frac{z_1}{z_m}}\,.$$

To overcome the nonphysical situation given by τ_{g0} values surpassing overall stress values, the density value to compute the effective velocity is bounded as $\rho_s \leq \rho_{\text{lim}} = 2\alpha\tau_*/g$. Hence we assume that any sediment overload ascribed to an excess of fluid transport capacity is instantly deposited on the bed. Note that this density limit is higher than the saturated density $\rho_{\text{sat}} = 2\alpha(\tau_* - \tau_t)/g$.

References

[1] R. Bravo, P. Ortiz, and J. Molina, "Modelling initial motion of non-spherical sediment particles on inclined and seeped beds," Appl. Math. Model. **96**, 678–696 (2021).
[2] R. Bravo, P. Ortiz, and J. Pérez, "Analytical and discrete solutions for the incipient motion of ellipsoidal sediment particles," J. of Hydr. Res. **56**, 29–43 (2018).
[3] G. Sauermann, K. Kroy, and H. Herrmann, "Continuum saltation model for sand dunes," Phys. Rev. E **64**, 031305 (2001).
[4] R. Bagnold, *The Physics of Blown Sand and Desert Dunes* (Methuen, London, 1941).
[5] H. Lettau and K. Lettau, "Exploring the world's driest climate. report of an expedition to pampa de la joya, peru, in july 1964," Tech. Rep. (Center for Climatic Research, U. of Wisconsin-Madison, 1978).
[6] P. Ortiz and P. Smolarkiewicz, "Coupling the dynamics of boundary layers and evolutionary dunes," Phys. Rev. E **79**, 041307–1–041307–11 (2009).
[7] O. Durán, B. Andreotti, and P. Claudin, "Numerical simulation of turbulent sediment transport, from bed load to saltation," Phys. Fluids **24**, 103306 (2012).

[8]J. Molina, P. Ortiz, and R. Bravo, "Fluid-evolving landform interaction by a surface-tracking method," Comput. Mech. **74**, 993–1008 (2024).
[9]J. Molina, P. Ortiz, and R. Bravo, "A finite element method for partially erodible bed evolution coupled with multiphase flows," Comput. Methods in Appl. Mech. Eng. **405**, 115853 (2023).
[10]P. Ortiz, "A positive definite continuous fem model for advection," Adv. Water Resour. **32**, 1359–1371 (2009).
[11]P. Ortiz, J. Anguita, and M. Riveiro, "Free surface flows over partially erodible beds by a continuous finite element method," Environ. Earth Sci. **74**, 7357–7370 (2015).
[12]J. Molina and P. Ortiz, "A continuous finite element solution of fluid interface propagation for emergence of cavities and geysering," Comput. Methods in Appl. Mech. Eng. **359**, 112746 (2020).
[13]P. Ortiz and P. Smolarkiewicz, "Numerical simulation of sand dune evolution in severe winds," Int. J. Numer. Meth. Fluids **50**, 1229–1246 (2006).
[14]R. Bravo, P. Ortiz, S. Idelsohn, and P. Becker, "Sediment transport problems by the particle finite element method (pfem)," Comput. Part. Mech. **7**, 139–149 (2020).
[15]M. Schmeeckle, "Numerical simulation of turbulence and sediment transport of medium sand," J. Geophys. Res. Earth Surf. **119**, 1240–1262 (2014).
[16]R. Sun and H. Xiao, "CFD–DEM simulations of current-induced dune formation and morphological evolution," Adv. Water Resour. **92**, 228–239 (2016).
[17]P. Ortiz, "Non-oscillatory continuous fem for transport and shallow water flows," Comput. Methods in Appl. Mech. Eng. **223–224**, 55–69 (2012).
[18]H. Selmani, A. Valance, O. El Moctar, P. Dupont, and R. Zegadi, "Aeolian sand transport in out-of-equilibrium regimes," Geophys. Res. Lett. **45**, 1838–1844 (2018).
[19]C. Groh, N. Wierschem, N. Aksel, I. Rehberg, and C. Kruelle, "Barchan dunes in two dimensions: Experimental tests for minimal models," Phys. Rev. E **78**, 021304 (2008).
[20]R. Anderson, "Wind modification and bed response during saltation of sand in air," Acta Mechanica **1**, 21–51 (1991).
[21]Z. Wang and M. Liu, "Semi-resolved CFD–DEM for thermal particulate flows with applications to fluidized beds," Int. J. Heat Mass Transf. **159**, 120150 (2020).
[22]L. van Rijn, "Sediment transport. part i: bed load transport," J. Hydraul. Eng.-ASCE **110**, 1431–1456 (1984).